A&A 541, A125 (2012)
DOI: 10.1051/0004-6361/201218867

Astronomy & Astrophysics

Potassium spectra in the 700–7000 cm^{-1} domain: Transitions involving f-, g-, and h-states

S. Civiš[1], M. Ferus[1], P. Kubelík[1], P. Jelinek[1], and V. E. Chernov[1,2]

[1] J. Heyrovský Institute of Physical Chemistry, Academy of Sciences of the Czech Republic, Dolejškova 3, 18223 Prague 8, Czech Republic
e-mail: civis@jh-inst.cas.cz
[2] Voronezh State University, 394693 Voronezh, Russia

Received 23 January 2012 / Accepted 28 February 2012

ABSTRACT

Context. The infrared (IR) range is becoming increasingly important to astronomical studies of cool or dust-obscured objects, such as dwarfs, disks, or planets, and in the extended atmospheres of evolved stars. A general drawback of the IR spectral region is the much lower number of atomic lines available (relative to the visible and ultraviolet ranges).
Aims. We attempt to obtain new laboratory spectra to help us identify spectral lines in the IR. This may result in the discovery of new excited atomic levels that are difficult to compute theoretically with high accuracy, hence can be determined solely from IR lines.
Methods. The K vapor was formed through the ablation of the KI (potassium iodide) target by a high-repetition-rate (1.0 kHz) pulsed nanosecond ArF laser (λ = 193 nm, output energy of 15 mJ) in a vacuum (10^{-2} Torr). The time-resolved emission spectrum of the neutral atomic potassium (K I) was recorded in the 700–7000 cm^{-1} region using the Fourier transform infrared spectroscopy technique with a resolution of 0.02 cm^{-1}. The f-values calculated in the quantum-defect theory approximation are presented for the transitions involving the reported K I levels.
Results. Precision laboratory measurements are presented for 38 K I lines in the infrared (including 25 lines not measured previously in the laboratory) range using time-resolved Fourier transform infrared spectroscopy. The 6g, 6h, and 7h levels of K I are observed for the first time, in addition to updated energy values of the other 23 K I levels and the f-values for the transitions involving these levels.
Conclusions. The recorded wave numbers are in good agreement with the data from the available solar spectrum atlases. Nevertheless, we correct their identification for three lines (1343.699, 1548.559, and 1556.986 cm^{-1}).

Key words. atomic data – line: identification – methods: laboratory – infrared: general – techniques: spectroscopic

1. Introduction

Understanding the chemical evolution of our Galaxy requires the determination of the element abundances in stars of different metallicities. Potassium is an odd-Z element that is mainly produced in massive stars by explosive oxygen burning (see Zhang et al. 2006b, and references therein).

An analysis of K abundances of 58 metal-poor stars (Zhang et al. 2006b) found that the dependence of [K/Fe] versus [Fe/H] agrees with the theoretical predictions of the chemical evolution models of the Galaxy. The spectroscopic determination of potassium abundances in metal-poor stars is difficult to obtain only because the resonance doublet (K I at 7665 Å and 7699 Å) lines are available in this analysis; moreover, these K I lines are often blended with very strong telluric O_2 lines.

Since it is one of the most important references in astronomy, the solar spectrum forms the basis of the description of the chemical evolution of our Galaxy. An analysis of the absorption lines found in the solar spectrum provides detailed information about the isotopic and elemental abundance distribution of a very large number of elements found in the solar system (Lodders 2003).

One of the most important problems of atmospheric line formation, is the assumption of local thermodynamic equilibrium (LTE), which is usually applied to the computation of atomic populations and radiative transfer (Gehren et al. 2001). Non-local thermal equilibrium (NLTE) occurs under high temperatures and low pressures, when the photon absorption rate exceeds the atom-electron collision rate. These conditions occur, for example, in metal-poor stars where electron collisions have lower rates because the free electron density is correlated with metal abundance (Gehren et al. 2001).

The level populations of the atoms with low ionization potentials are particularly sensitive to deviations from LTE. As for other atoms with one electron in the outermost shell, K I has one of the lowest ionization energies (4.34 eV) in the periodic system. Neutral sodium constitutes approximately 0.7% of the sodium atoms under the conditions of the solar photosphere, whereas neutral potassium represents only 0.1%. The photospheric solar potassium abundance based on the theoretical NLTE model atmospheres is $\log \varepsilon_{\odot}(K) = 5.12 \pm 0.03$ (Zhang et al. 2006a); the Fe abundance is also calculated by accounting for NLTE (Gehren et al. 2001). There are several stellar atmosphere models that predict different photospheric/coronal abundance ratios as a function of ionization potential. Hence, K I abundance can be used to test these models for different stars. For instance, CORONAS-F solar spacecraft measurements (Sylwester et al. 2010) yielded possible values of the coronal abundance of K with a peak at $\log \varepsilon_{\odot}(K) = 5.86$ and a half-peak range of 5.63–6.09. The latter measurements were based on the resonant line of the He-like K (K XVIII) ion in the X-ray range.

In addition to the optical, UV, and X-ray ranges, the infrared (IR) range is becoming increasingly important to astronomical research, for instance in studies of dust-obscured objects and interstellar clouds, cool objects such as dwarfs, disks, or planets and the extended atmospheres of evolved stars, including objects at cosmological distances from the Earth (Kerber et al. 2009).

The IR spectrum of the most studied object, the Sun, has been recorded from the ground (Wallace et al. 1996) and the stratosphere (Goldman et al. 1996), but, even in the atmospheric window regions, the recorded spectra contain many telluric atmosphere absorption lines. Pure solar IR spectra were recorded by the ATMOS (Atmospheric Trace Molecule Spectroscopy) Fourier transform spectrometer (FTS) during four Space Shuttle missions (Farmer et al. 1989) in the 600–4800 cm^{-1} range at a resolution of 0.01 cm^{-1} ($R = \lambda/\Delta\lambda \sim 6 \times 10^4$–$5 \times 10^5$). A more recent program, the Atmospheric Chemistry Experiment with a space-borne FTS (ACE-FTS), has been performed on board a SCISAT-1 satellite (Hase et al. 2010). The ACE solar atlas covers the 700–4430 cm^{-1} frequency range at a resolution of 0.02 cm^{-1} ($R \sim 2 \times 10^4$–2×10^5).

The current space-born spectrographs performing IR studies of objects other than the Sun, have lower spectral resolutions. The *Spitzer* Space Telescope has a resolution of $R \sim 600$ in the $\lambda = 10$–37 micron range (Houck et al. 2004); the AKARI satellite (Murakami et al. 2007) is equipped with a Far-Infrared Surveyor (FTS with resolution $\Delta\nu = 0.19$ cm^{-1}) and a near- and mid-IR camera with a resolution of up to $\Delta\lambda = 0.0097$ microns ($R \sim 100$–1000). Nevertheless, the forthcoming spatial and airborne telescopes are expected to have a much higher resolution. For instance, the airborne Stratospheric Observatory For Infrared Astronomy (SOFIA) (Gehrz et al. 2009) is planned to be complemented with the Echelon-cross-Echelle Spectrograph (EXES) with a resolution of $R \sim 10^5$ in the wavelength region of 4.5 to 28.3 microns (Richter et al. 2010). The future SPace Infrared telescope for Cosmology and Astrophysics (SPICA) (Goicoechea et al. 2011) will carry a mid-IR, high resolution spectrometer (MIRHES) operating in the 4–18 micron range with a spectral resolution of $R \sim 3 \times 10^4$.

The great advantages of Fourier transform infrared spectroscopy (FTIR), such as its constant high resolution and energy throughput, have made the IR spectral region more accessible for laboratory spectral measurements (Nilsson 2009). Nevertheless, the powerful capacities of IR astronomy, including the existing VLT with CRyogenic Infra-Red Echelle Spectrograph, (CRIRES) and the future ground-based (e.g., E-ELT) or satellite-borne (e.g., Gaia, 0.33–1.05 micron range) IR telescopes, cannot be fully utilized without detailed spectroscopic information on atomic line features (in particular, wavelengths and oscillator strengths) in the IR region (Biémont 1994; Grevesse & Noels 1994; Pickering 1999; Jorissen 2004; Johansson 2005; Pickering et al. 2011).

A general drawback of the IR spectral region is the much lower number of atomic and ionic lines available (relative to the visible and ultraviolet ranges) (Ryde 2010). Modern laboratory spectral features are lacking for most elements with wavelengths longer than 1 micron (Wahlgren 2011). On the other hand, atlases of stellar spectra often provide only a short list of identified lines (Lobel 2011). Even in the solar IR atlas (Hase et al. 2010), there are a number of lines with doubtful or missing identifications.

New laboratory spectra may help us to identify spectral lines in IR and potentially discover new excited atomic levels. These levels are difficult to compute with high accuracy theoretically, hence they can be determined solely from IR lines (Wahlgren 2011). The inclusion of additional atomic lines and higher energy levels will increase the reliability of astrophysical calculations such as stellar atmosphere models. For instance, modern analyses of solar chemical compositions (Asplund et al. 2009) measure substantially lower metallicities than determined two decades ago. The use of high-resolution solar spectra (Hase et al. 2010) for the computation of the Sun's irradiance spectrum is still in its initial stage of development (Kurucz 2011).

The above-mentioned development of IR astronomy, together with the lack of high-resolution laboratory data for atomic spectral features, illustrates the importance of reporting new IR atomic lines, highly-excited levels, and oscillator strengths. For instance, the identification of IR atomic lines may be used for reliable temperature, gravity, and abundance analyses for a wide range of ultra-cool dwarfs, from M dwarf stars to brown dwarfs as well as extra-solar giant planets (Lyubchik et al. 2004). A comparison of these atomic lines with computed profiles can be used as key diagnostics of ultra-cool dwarf atmospheres (Lyubchik et al. 2007). Laboratory-measured manganese IR line features were used to determine the Mn abundance in the atmospheres of the Sun, Arcturus, and a dwarf (Blackwell-Whitehead et al. 2011). Together with the molecular IR bands, atomic (including K I) IR lines provide good diagnostics for a self-consistent pure-infrared spectral classification scheme in most cases for both L and T dwarfs (McLean et al. 2003). The investigation of the gravity-sensitive features of atomic (including K I) IR line features was used as a way to distinguish between young and old brown dwarfs (McGovern et al. 2004). Even without a direct application to the stellar atmosphere and abundance models, information on atomic spectral features is in constant demand from the astrophysical community (Raassen et al. 1998; Blackwell-Whitehead et al. 2005; Wallace & Hinkle 2007; Brown et al. 2009; Wallace & Hinkle 2009; Deb & Hibbert 2010; Thorne et al. 2011).

Parts of the spectra in the 800–1800 cm^{-1} (12.5–5.6 microns) range are difficult to observe from the ground owing to the heavy contamination of the spectrum by telluric absorption lines. This infrared spectrum represents a great challenge for laboratory observations of new, unknown infrared atomic transitions involving atomic levels with a high orbital momentum (Civiš et al. 2011b) and their comparison with the available stellar (e.g., solar) spectra. An attempt to fill this gap for K I is made in the present paper.

After K I spectrum measurements were made by Risberg (1956) in the 0.3101–1.1772 μm range a half of century ago, potassium IR lines were reported by Johansson & Svendenius (1972) who extended the measurements up to 3.735 μm and by Litzen (1970) who reported the 5g-levels of K I from his measurement of 4.0169 μm line. In these hollow-cathode measurements, no lines with longer wavelengths were recorded, nor was emission from ng (with $n > 5$) or nh-levels observed. Here, we report the results of a FTIR spectroscopy study of K I transitions in the following IR ranges: 1.4–2.5, 2.7–5.0, 5.9–9.1 and 11.1–14.3 microns.

2. Method

Time-resolved FTIR spectroscopy was applied to observing the emission arising after the irradiation of a potassium iodine (KI) target with a pulsed nanosecond ArF ($\lambda = 193$ nm) laser. A high-repetition-rate ArF laser ExciStar S-Industrial V2.0 1000 (193 nm, laser pulse width 12 ns, frequency 1 kHz) with 15 mJ pulse energy was focused on a rotating and linearly traversing target (CsI tablet) with a vacuum chamber (average pressure 10^{-1} Torr). The IR emission of the laser plume was measured

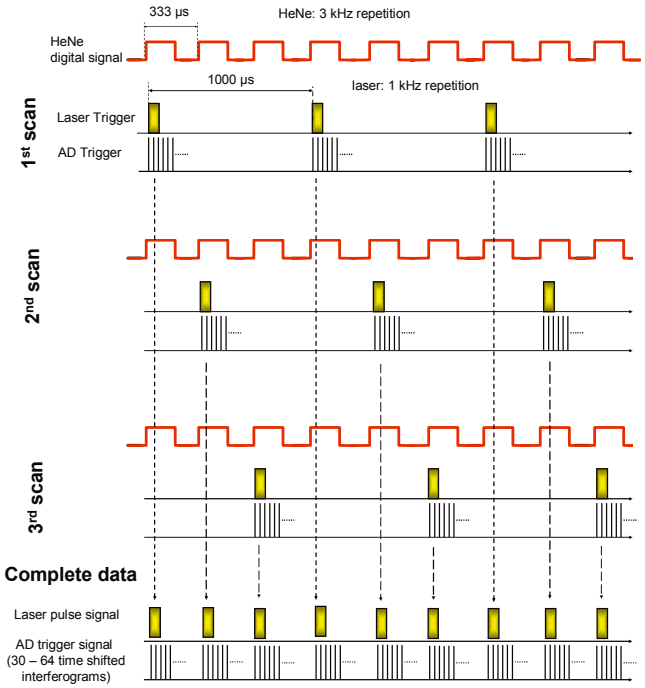

Fig. 1. Timing diagram for the interleaved sampling. During the scan, the laser pulse and the AD trigger sampling are induced with a rate of $1/n$ times of the He–Ne laser fringe frequency. The complete interferograms are obtained after n scans ($n = 3$ here).

in the probed area at an axial distance of $L = 9$ mm from the target. The emission from this area was focused into the spectrometer by CaF_2 (100 mm) or ZnSe (127 mm) lenses (for the 1600–7700 cm^{-1} or 800–1600 cm^{-1} spectral ranges, respectively). Two different detectors (MCT and InSb) and two beamsplitters (KBr and CaF_2) were used to cover the measured spectral range. The measurements were performed with a resolution of 0.017 cm^{-1}.

The continuous scanning method was used to measure the time-resolved FTIR spectra. After each ArF laser trigger point, several data points were sampled during the continual movement of the interferometer mirror. The synchronization of the laser ablation, which is the source of the emission, with the signal acquisition requires a special technique. In the case of the common time-resolved FT measurement, the time-shifted signals from a detector are sampled at each zero-crossing point of the HeNe laser fringes. A complication is that the repetition rate lasers suitable for ablation experiments is lower then the frequency of the HeNe laser fringes produced by the interferometer. Therefore, the laser pulse is triggered only in the chosen (every second, third, or fourth etc.) zero-cross point of the HeNe laser fringes. As a result, $1/n$ of each time-resolved interferogram is obtained after each scan Kawaguchi et al. (2005). The timing diagram is shown in Fig. 1, where the time sequence corresponds to the case of $n = 3$; several measurements were performed with the divider $n = 4$. An assembly of the n parts of the interferogram sampled at the same time after the laser pulse provides the complete interferogram. The output of this process is a set of time-resolved interferograms (30–64).

Our system was designed using a field programable gate array (FPGA) processor. The main role of the FPGA processor in our experiment was to initiate a laser pulse and AD trigger signals (the signal for data collection from the detector) synchronously with the He–Ne laser fringe signals from the spectrometer. The FPGA processor also controls the data transmission from the digital input board to the PC. The width of the ablation laser pulse, as well as the offset value between the beginning of the laser pulse and the data acquisition, can be preset.

In the present experiments, we used a 60 μs offset followed by the 30 AD trigger acquisition signals covering a 30 μs interval. The matrix of data signals corresponding to the AD triggers was stored and Fourier-transformed. The acquired interferograms were post-zerofilled using the OPUS Bruker program OPUS (2010) and subsequently corrected by subtracting the blackbody background spectrum. The wavenumbers, line widths, and their intensities were then obtained using the OPUS peak picking procedure. For more details of the experimental setup, we refer to our previous papers (Civiš et al. 2010a; Kawaguchi et al. 2008).

The use of the time-resolved scheme is essential because the emission intensities of the spectral lines depend on the time delay after the ArF laser pulse shot. The maxima of time profiles of the emission lines arise at different delay times $\tau \simeq 3$–10 μs, hence one should examine a wide time-domain range (0–30 μs) to avoid missing a line in the resulting spectra. The intensities reported in Table 1 below were obtained as the emission values at the time profile maxima. This non-monotonic decay of the emission intensity could be due to the complex population kinetics of the atomic K I states in the ablation plasma.

Such a complex system was not solely used to excite the spectrum of a neutral atom. Although inexpensive potassium hollow cathode lamps are commercially available, they are apparatuses of quite moderate power used mostly with visible range optics. Their usage in the IR requires substantial modifications (e.g., IR optics and windows). We note that previous hollow-cathode studies of the K I spectrum did not report many of the IR lines that are listed in this work. In addition, our scheme was designed to perform measurements of the IR spectra of several targets, not solely potassium (see our previous results, Civiš et al. 2010a; Civiš et al. 2010b, 2011b).

In this paper we record FTIR spectra in the five spectral ranges of 700–900, 1100–1700, 2000–3700, 4100–5000 and 5000–7000 cm^{-1} (11–14, 5.9–9.1, 2.7–5.0, 2.0–2.4 and 1.4–2.0 μm, respectively). An InSb detector was used for all spectral domains except the 700–900 and 1100–1700 cm^{-1} domain, where an MCT detector was used. All of the observed emission lines were classified as to transitions between $3p^6\ nl_j$ K I levels with $n = 3...7$ and $l = 0...4$. No halogen (Cl, Br, F or I) lines were observed in the recorded emission spectra. The spectral resolution was either 0.1 cm^{-1} (four scans, higher signal-to-noise ratio (S/N)) or 0.017 cm^{-1} (one scan, lower S/N). The acquired interferograms were post-zerofilled (zero filling 2, trapezoid apodization function, for details see, e.g., the book by Stuart 2004) using Bruker OPUS software and subsequently corrected by subtracting the blackbody background spectrum.

The results of the line measurement and assignment are presented in Table 1. The wavenumbers, line widths, and their intensities (as well as the uncertainties in these quantities) were obtained by fitting a Lorentzian line shape.

To identify the observed lines, we assumed that, under LTE conditions and negligible self-absorption (optically thin plasma), the intensity of a spectral line due to radiative transition from the upper state $|k\rangle$ to the lower state $|i\rangle$ is proportional to the line strength S_{ik}, which is related to the oscillator strength f_{ik} according to $S_{ik} = \dfrac{3\hbar e^2 g_i}{2m_e\omega_{ik}} f_{ik}$ (Larsson 1983), where ω_{ik} is 2π multiplied by the transition frequency, g_i is the degeneracy factor of the lower level, and m_e and e are the electron mass and

Table 1. K I lines and their identification.

Present work					Other measurements[a]		
Wavenumber (cm^{-1})	Wavelength (μm)	Intensity (arb. units)	S/N	HWHM (cm^{-1})	Identification	Laborat.	ACE [3][b]
729.694(8)	13.7006	1.41×10^4	5.32	0.057(26)	$4d_{\frac{3}{2}}$–$4f_{\frac{5}{2}}$		
730.755(6)	13.6807	1.10×10^4	5.04	0.048(37)	$4d_{\frac{5}{2}}$–$4f_{\frac{7}{2}}$		
795.575(16)	12.5661	5.98×10^3	3.34	0.049(60)	$7s_{\frac{1}{2}}$–$7p_{\frac{1}{2}}$		
800.081(12)	12.4953	1.15×10^4	5.38	0.047(32)	$7s_{\frac{1}{2}}$–$7p_{\frac{3}{2}}$		
809.189(12)	12.3547	2.15×10^4	4.33	0.107(39)	6g –7h		
884.125(11)	11.3075	1.63×10^4	4.62	0.073(38)	$5d_{\frac{3}{2}}$–$7p_{\frac{1}{2}}$		
889.117(8)	11.2441	2.55×10^4	7.70	0.075(22)	$5d_{\frac{5}{2}}$–$7p_{\frac{3}{2}}$		
1177.545(3)	8.489930	1.86×10^5	35.5	0.083(9)	$6p_{\frac{3}{2}}$–$5d_{\frac{5}{2}}$		NA / NA /.55
1178.041(13)	8.486355	1.66×10^4	2.97	0.066(57)	$6p_{\frac{3}{2}}$–$5d_{\frac{3}{2}}$		
1186.478(2)	8.426009	1.00×10^5	34.9	0.071(9)	$6p_{\frac{1}{2}}$–$5d_{\frac{3}{2}}$		
1266.577(4)	7.893144	6.16×10^4	17.6	0.073(11)	$6p_{\frac{3}{2}}$–$7s_{\frac{1}{2}}$		
1275.007(3)	7.840956	3.30×10^4	14.2	0.061(15)	$6p_{\frac{1}{2}}$–$7s_{\frac{1}{2}}$		
1343.699(4)	7.440114	1.61×10^5	16.1	0.136(13)	5g –6h		.702/.698/.703 (Mg I 6g ^{3}G–8h ^{3}H)
1352.873(5)	7.389662	5.34×10^4	8.72	0.106(17)	5f –6g		
1548.559(5)	6.455856	1.17×10^5	5.10	0.097(17)	$6s_{\frac{1}{2}}$–$6p_{\frac{1}{2}}$		.566/.561/.564 (CO 12–11)
1556.986(4)	6.420915	2.10×10^5	15.0	0.096(11)	$6s_{\frac{1}{2}}$–$6p_{\frac{3}{2}}$		.99/.986/ NA (unassigned)
1601.103(3)	6.243992	9.40×10^4	16.6	0.091(11)	$4d_{\frac{3}{2}}$–$6p_{\frac{1}{2}}$		
1609.533(12)	6.211289	1.60×10^4	2.60	0.083(54)	$4d_{\frac{3}{2}}$–$6p_{\frac{3}{2}}$		
1610.601(3)	6.207170	1.72×10^5	30.5	0.093(10)	$4d_{\frac{5}{2}}$–$6p_{\frac{3}{2}}$		
2057.382(8)	4.859221	8.97×10^2	3.79	0.078(24)	$4f_{\frac{7}{2}}$–$5d_{\frac{5}{2}}$		
2057.898(15)	4.858003	7.69×10^2	2.68	0.086(54)	$4f_{\frac{5}{2}}$–$5d_{\frac{3}{2}}$		
2489.439(3)	4.015874	5.40×10^4	7.92	0.111(8)	4f –5g	.462 [1]	.446/.438/.46
2676.927(4)	3.734608	1.11×10^5	4.16	0.126(12)	$5p_{\frac{3}{2}}$–$4d_{\frac{5}{2}}$	.938 [2]	.936/.928/.938
2678.012(10)	3.733095	8.23×10^3	2.88	0.105(34)	$5p_{\frac{3}{2}}$–$4d_{\frac{3}{2}}$	.008 [2]	.011/.003/.008
2696.757(3)	3.707147	6.08×10^4	4.23	0.123(11)	$5p_{\frac{1}{2}}$–$4d_{\frac{3}{2}}$	.765 [2]	.767/.759/.765
2730.542(3)	3.661278	2.87×10^4	5.09	0.118(10)	$5p_{\frac{3}{2}}$–$6s_{\frac{1}{2}}$	.554 [2]	.556/.548/.571
2749.299(3)	3.636299	1.43×10^4	6.01	0.115(11)	$5p_{\frac{1}{2}}$–$6s_{\frac{1}{2}}$	.309 [2]	.283/.274/.328
3164.389(4)	3.159306	3.38×10^4	5.07	0.118(11)	$3d_{\frac{3}{2}}$–$5p_{\frac{1}{2}}$	.396 [2]	.401/.392/.394
3183.135(4)	3.140700	6.32×10^3	4.11	0.112(14)	$3d_{\frac{3}{2}}$–$5p_{\frac{3}{2}}$	.153 [2]	.154/.144/.151
3185.455(3)	3.138413	6.34×10^4	5.00	0.118(10)	$3d_{\frac{5}{2}}$–$5p_{\frac{3}{2}}$	.461 [2]	.467/.458/.459
3208.542(7)	3.115831	5.11×10^3	3.36	0.104(21)	$4d_{\frac{3}{2}}$–$5f_{\frac{5}{2}}$		NA / NA /.583
3209.628(4)	3.114776	9.90×10^3	5.68	0.120(14)	$4d_{\frac{5}{2}}$–$5f_{\frac{7}{2}}$		NA / NA /.653
3674.823(7)	2.720477	1.03×10^3	6.10	0.088(20)	$5s_{\frac{1}{2}}$–$5p_{\frac{1}{2}}$	.827 [2]	.825/.814/.831
3693.570(4)	2.706669	5.37×10^3	5.20	0.107(12)	$5s_{\frac{1}{2}}$–$5p_{\frac{3}{2}}$	.585 [2]	.58 /.569/.586
4555.000(8)	2.194791	2.94×10^4	2.99	0.058(36)	$4d_{\frac{3}{2}}$–$6f_{\frac{5}{2}}$		
4556.057(11)	2.194281	5.55×10^4	3.83	0.095(38)	$4d_{\frac{5}{2}}$–$6f_{\frac{7}{2}}$		
6590.857(10)	1.516839	1.87×10^5	6.51	0.069(16)	$3d_{\frac{3}{2}}$–$4f_{\frac{5}{2}}$		
6593.169(3)	1.516307	2.39×10^5	8.89	0.069(9)	$3d_{\frac{5}{2}}$–$4f_{\frac{7}{2}}$		

Notes. Each of the five spectral ranges (700–900, 1100–1700, 2000–3700, 4100–5000, and 5000–7000 cm^{-1}) has its own scale of arbitrary units for the emission intensity. [(a)] Only the fractional part of the wavenumbers in cm^{-1}. [(b)] Data format: line list 1 (corrected)/line list 1 (observed)/line list 2 (see Hase et al. 2010, Sect. 4). NA means that the line is not listed in the corresponding line list.

References. [1] Johansson & Svendenius (1972); [2] Litzen (1970); [3] Hase et al. (2010).

charge, respectively. When LTE is fulfilled and self-absorption is negligible (or properly taken into account), the f-values can be determined from the laser-ablation plasma spectra if the temperature of the atom energy distribution is known (Manrique et al. 2011).

Since the atom concentration is low at the low pressures used in our experiment, we can consider our plasma to be optically thin. However, under the same conditions, some deviations from LTE conditions can occur, but the Boltzmann distribution of the atomic populations remains valid (Giacomo et al. 2001), though with different temperatures for electrons and atoms. This means that even if the observed line intensities display some deviations from the proportionality to the S-values, they should describe the qualitative picture of the relative line intensities adequately enough to assign the lines. A typical example of a Boltzmann plot for the ablation plasma can be found in Civiš et al. (2011a). The uncertainty in the excitation temperature is small enough to consider the Boltzmann population distribution to be a satisfactory approximation for our experiment. The moderate deviation of the Boltzmann plot's points away from the straight line

Table 2. Comparison of the QDT-calculated (this work) K I oscillator strengths with other works.

Transition	ν (cm^{-1})	λ (μ)m	$\log(g_i f_{ik})$	f_{ik}	
$4s_{\frac{1}{2}}$–$10p_{\frac{3}{2}}$	33 411.3986	0.299211788	−10.8	1.00×10^{-5}	8.46×10^{-6} [1]
$4s_{\frac{1}{2}}$–$10p_{\frac{1}{2}}$	33 410.2306	0.299222249	−12.	3.22×10^{-6}	2.91×10^{-6} [1]
$4s_{\frac{1}{2}}$–$9p_{\frac{3}{2}}$	32 941.9262	0.303476190	−10.1	1.99×10^{-5}	1.86×10^{-5} [1]
$4s_{\frac{1}{2}}$–$9p_{\frac{1}{2}}$	32 940.203	0.30349207	−11.2	6.78×10^{-6}	6.6×10^{-6} [1]
$4s_{\frac{1}{2}}$–$8p_{\frac{3}{2}}$	32 230.11	0.3101789	−9.29	4.62×10^{-5}	4.68×10^{-5} [1]
$4s_{\frac{1}{2}}$–$8p_{\frac{1}{2}}$	32 227.44	0.3102046	−10.3	1.69×10^{-5}	1.76×10^{-5} [1]
$4s_{\frac{1}{2}}$–$7p_{\frac{3}{2}}$	31 074.4	0.321715	−8.21	1.36×10^{-4}	1.54×10^{-4} [1]
$4s_{\frac{1}{2}}$–$7p_{\frac{1}{2}}$	31 069.9	0.321762	−9.14	5.37×10^{-5}	6.18×10^{-5} [1]
$4s_{\frac{1}{2}}$–$6p_{\frac{3}{2}}$	29 007.71	0.3446372	−6.74	5.91×10^{-4}	5.92×10^{-4} [1]
$4s_{\frac{1}{2}}$–$6p_{\frac{1}{2}}$	28 999.27	0.3447375	−7.6	2.51×10^{-4}	2.58×10^{-4} [1]
$4s_{\frac{1}{2}}$–$5p_{\frac{3}{2}}$	24 720.139	0.40441422	−4.53	5.40×10^{-3}	5.69×10^{-3} [1]
$4s_{\frac{1}{2}}$–$5p_{\frac{1}{2}}$	24 701.382	0.40472132	−5.31	2.48×10^{-3}	2.63×10^{-3} [1]
$4p_{\frac{1}{2}}$–$9d_{\frac{3}{2}}$	20 586.9392	0.485609209	−5.92	1.34×10^{-3}	1.3×10^{-3} [2]
$4p_{\frac{3}{2}}$–$9d_{\frac{3}{2}}$	20 529.2289	0.486974338	−7.49	1.39×10^{-4}	1.2×10^{-4} [2]
$4p_{\frac{3}{2}}$–$9d_{\frac{5}{2}}$	20 529.1632	0.486975896	−5.29	1.26×10^{-3}	1.1×10^{-3} [2]
$4p_{\frac{1}{2}}$–$10s_{\frac{1}{2}}$	20 229.041	0.49420087	−6.26	9.52×10^{-4}	7.8×10^{-4} [2]
$4p_{\frac{1}{2}}$–$8d_{\frac{3}{2}}$	20 193.0467	0.495081800	−5.63	1.79×10^{-3}	1.6×10^{-3} [2]
$4p_{\frac{3}{2}}$–$10s_{\frac{1}{2}}$	20 171.3307	0.495614801	−5.58	9.47×10^{-4}	7.83×10^{-4} [2]
$4p_{\frac{3}{2}}$–$8d_{\frac{3}{2}}$	20 135.3364	0.496500783	−7.2	1.86×10^{-4}	1.7×10^{-4} [2]
$4p_{\frac{3}{2}}$–$8d_{\frac{5}{2}}$	20 135.2379	0.496503212	−5.	1.68×10^{-3}	1.4×10^{-3} [2]
$4p_{\frac{1}{2}}$–$9s_{\frac{1}{2}}$	19 663.1654	0.508423398	−5.79	1.53×10^{-3}	1.36×10^{-3} [2]
$4p_{\frac{1}{2}}$–$7d_{\frac{3}{2}}$	19 613.258	0.50971714	−5.35	2.38×10^{-3}	2.3×10^{-3} [2]
$4p_{\frac{3}{2}}$–$9s_{\frac{1}{2}}$	19 605.4551	0.509920004	−5.1	1.52×10^{-3}	1.4×10^{-3} [2]
$4p_{\frac{3}{2}}$–$7d_{\frac{3}{2}}$	19 555.5477	0.511221379	−6.92	2.48×10^{-4}	2.2×10^{-4} [2]
$4p_{\frac{3}{2}}$–$7d_{\frac{5}{2}}$	19 555.3921	0.511225447	−4.71	2.24×10^{-3}	2.1×10^{-3} [2]
$4p_{\frac{1}{2}}$–$8s_{\frac{1}{2}}$	18 780.191	0.53232786	−5.22	2.71×10^{-3}	2.7×10^{-3} [2]
$4p_{\frac{3}{2}}$–$8s_{\frac{1}{2}}$	18 722.4807	0.533968732	−4.53	2.70×10^{-3}	2.69×10^{-3} [2]
$4p_{\frac{1}{2}}$–$6d_{\frac{3}{2}}$	18 710.9804	0.534296928	−5.13	2.96×10^{-3}	3.4×10^{-3} [2]
$4p_{\frac{3}{2}}$–$6d_{\frac{3}{2}}$	18 653.2701	0.535949978	−6.69	3.10×10^{-4}	3.3×10^{-4} [2]
$4p_{\frac{3}{2}}$–$6d_{\frac{5}{2}}$	18 653.0045	0.535957610	−4.49	2.81×10^{-3}	3.0×10^{-3} [2]
$4p_{\frac{1}{2}}$–$7s_{\frac{1}{2}}$	17 289.063	0.57823999	−4.47	5.71×10^{-3}	6.17×10^{-3} [2]
$4p_{\frac{3}{2}}$–$7s_{\frac{1}{2}}$	17 231.3527	0.580176621	−3.78	5.68×10^{-3}	6.21×10^{-3} [2]
$4p_{\frac{1}{2}}$–$5d_{\frac{3}{2}}$	17 200.5619	0.581215207	−5.29	2.52×10^{-3}	2.8×10^{-3} [2]
$4p_{\frac{3}{2}}$–$5d_{\frac{3}{2}}$	17 142.8516	0.583171849	−6.82	2.72×10^{-4}	2.8×10^{-4} [2]
$4p_{\frac{3}{2}}$–$5d_{\frac{5}{2}}$	17 142.3479	0.583188985	−4.62	2.47×10^{-3}	2.4×10^{-3} [2]
$4p_{\frac{1}{2}}$–$6s_{\frac{1}{2}}$	14 465.5247	0.691108150	−3.38	1.71×10^{-2}	1.95×10^{-2} [2]
$4p_{\frac{1}{2}}$–$4d_{\frac{3}{2}}$	14 412.961	0.69362862	−7.08	4.19×10^{-4}	3.8×10^{-4} [2]
$4p_{\frac{3}{2}}$–$4d_{\frac{3}{2}}$	14 355.251	0.69641712	−9.04	2.96×10^{-5}	3.7×10^{-5} [2]
$4p_{\frac{3}{2}}$–$4d_{\frac{5}{2}}$	14 354.181	0.69646903	−6.88	2.56×10^{-4}	3.4×10^{-4} [2]
$4s_{\frac{1}{2}}$–$4p_{\frac{3}{2}}$	13 042.896027	0.76648991044	+0.162	5.88×10^{-1}	6.7×10^{-1} [3]
$4s_{\frac{1}{2}}$–$4p_{\frac{1}{2}}$	12 985.185724	0.76989645407	−0.534	2.93×10^{-1}	3.33×10^{-1} [3]
$4p_{\frac{1}{2}}$–$3d_{\frac{3}{2}}$	8551.802	1.169024	+0.536	8.55×10^{-1}	9.02×10^{-1} [2]
$4p_{\frac{3}{2}}$–$3d_{\frac{3}{2}}$	8494.092	1.176967	−1.07	8.54×10^{-2}	9.02×10^{-2} [2]
$4p_{\frac{3}{2}}$–$3d_{\frac{5}{2}}$	8491.784	1.177287	+1.12	7.69×10^{-1}	8.08×10^{-1} [2]
$4p_{\frac{1}{2}}$–$5s_{\frac{1}{2}}$	8041.365	1.243230	−1.07	1.71×10^{-1}	1.8×10^{-1} [2]
$4p_{\frac{3}{2}}$–$5s_{\frac{1}{2}}$	7983.655	1.252217	−0.374	1.72×10^{-1}	1.83×10^{-1} [2]

References. [1]: Shabanova & Khlyustalov (1985a,b); [2]: Villars (1952); [3]: Wang et al. (1997).

can be considered as evidence that S_{ik} values are calculated with enough accuracy (at least to confirm our line identifications).

Using K I atomic-level energy data (Ralchenko et al. 2011, and references therein), we checked all of the transitions in the 700–7000 cm^{-1} range allowed by the electric dipole rules. In the cases of transitions with close wavenumbers, we chose those with greater line strength. For the calculation of the oscillator strengths, we used single-channel quantum defect theory (QDT), which has proved its efficiency for the calculation of first- (Alcheev et al. 2002) and second- (Chernov et al. 2005; Akindinova et al. 2009) order matrix elements in atoms and molecules. We tested our QDT technique by comparing the QDT calculations with the experimental oscillator strengths available at NIST (Ralchenko et al. 2011). The results of this comparison

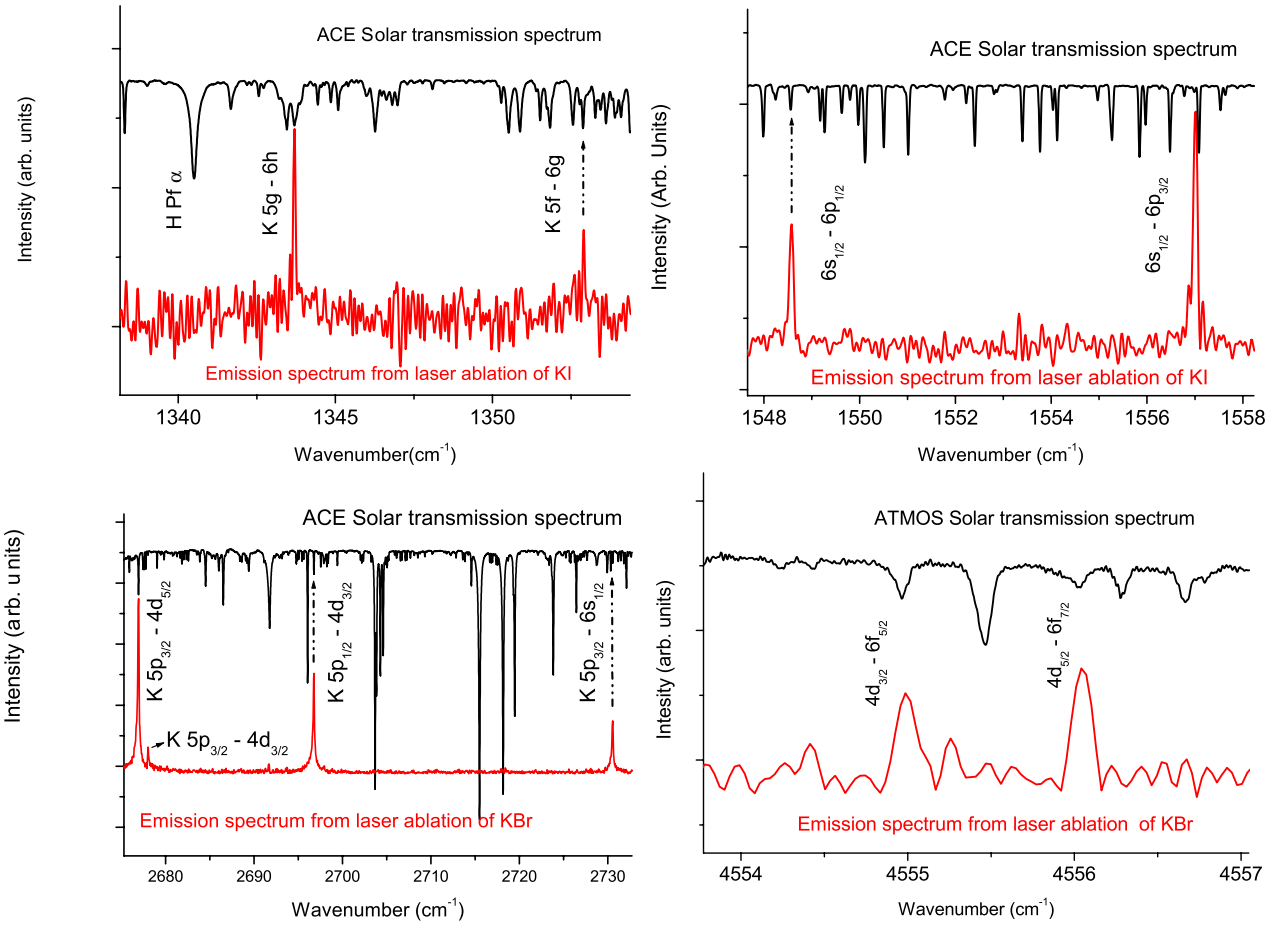

Fig. 2. K I emission spectra from the ablation plasma and the Solar spectra recorded from space-born spectrometers.

are presented in Table 2 with references to the original papers. For the majority of K I transitions, the QDT calculations indicate that there is closer agreement with the experimental data of Ralchenko et al. (2011) than the Fues model potential used in our previous works (Civiš et al. 2010a; Civiš et al. 2010b, 2011c). There are a number of other (not listed in Table 2) transitions for which only theoretical f-values are available at NIST. These values were calculated (Anderson & Zilitis 1964) using the Coulomb approximation (CA), which is somewhat similar to the QDT and FMP techniques. Some of these CA f-values are closer to our FMP values than QDT calculations. We do not present these large data lists here, and give these CA values only for the transitions between the K I levels observed in the present work, which are listed in Table 3. This table was used to classify the observed lines.

After classification, we refined the energy values for some levels involved in the assigned transitions. To this end, we applied a procedure similar to that used in our previous studies (Civiš et al. 2010b, 2011c,b). Table 4 presents some K I revised energy values, E_i, and their uncertainties.

3. Results

The FTIR spectra of K I were recorded in five spectral regions (700–900, 1100–1700, 2000–3700, 4100–5000, and 5000–7000 cm^{-1}). The measured emission lines are presented in Table 1 (with different intensity unit scales for different spectral regions). This table also contains the wavenumbers of some K I lines in the above spectral regions measured both in the laboratories (Litzen 1970; Johansson & Svendenius 1972) and space (the ACE-FTS solar atlas described by Hase et al. 2010). The ACE-FTS spectral data actually represented as three data lists. The second data list (according to Hase et al. 2010) contains the set of wavenumbers and transitions specified in the graphic ACE atlas pages. A simple analysis shows that the K I line wavenumbers encountered in the data list 2 are simply the Ritz wavenumbers obtained from the K I level energies stored in the NIST database (Ralchenko et al. 2011). The first data list is presented in two variants: (a) the list of observed lines and (b) the corrected (by an empirical calibration factor of 1.00000294) version of the observed data; the correction was made to achieve closer agreement with the line positions specified in the second data list. All three variants (list 1 corrected, list 1 observed and list 2) are compared in Table 1 with the K I lines observed in the present work.

We consider the ACE data list 1 (uncorrected) to be the most relevant to compare with our results since the above correction (by a calibration factor of 1.00000294) was performed in the ACE atlas (Hase et al. 2010) to aid the assignment of the spectral signatures in the ACE solar spectrum with the line positions given in current spectroscopic line-lists. The uncertainty in ACE peak picking is 0.001 cm^{-1}, which is better than those of our lines. At the same time, for a number of lines our uncertainties are better than those of the previous laboratory measurements, including the values of 0.005 cm^{-1} in Johansson & Svendenius (1972) and 0.01 cm^{-1} in Litzen (1970). Both of these previous laboratory measurements and our results coincide with ACE data within the corresponding uncertainties. However, our wavenumbers are generally closer to those of ACE compared to the wavenumbers from the previous measurements (Johansson & Svendenius 1972; Litzen 1970).

Some parts of the measured emission spectra in the vicinity of the most prominent lines are shown in Fig. 2 (upper red curve), together with the ACE-FTS or ATMOS solar transmission spectra (upper black curve) in the corresponding ranges. The majority of our emission peaks are lined up with the closest ACE features. As shown in Table 1, the majority of the line wavenumbers measured in the present work in the 2000–3700 cm^{-1} range are in good agreement (within 0.01 cm^{-1}) with the values from the non-corrected list 1 of ACE. The spectral regions (4100–5000 and 5000–7000 cm^{-1}) are not covered by the ACE atlas. In the 1100–1700 cm^{-1} range, the most prominent line observed in the present work is the 1343.699 cm^{-1} line. According to Table 3, this line should be the most prominent for all of the spectral ranges considered. The ACE data list 2 attributes its identification to the Mg I 6g^{3}G–8h^{3}H transition. This is probably incorrect since the ACE data list 2 identification is based only on a Ritz wavenumber obtained from the NIST database (Hase et al. 2010, Table 3). However, to our knowledge, there has been no report of a measured Mg I line near 1343.7 cm^{-1}. Moreover, our preliminary FTIR measurements in the laser ablation of magnesium salts do not show an Mg line at this position. Thus, we consider that the solar 1343.699 cm^{-1} line belongs to K I according to Table 1.

The revised energy values of the K I levels obtained from the present measurement are presented in Table 4. The majority of the energies coincide with the previously reported values within the uncertainty limits. Given the smaller (as compared to the previous measurements) uncertainty in our values for f-, g-, and 7p-level energies, the revised energy values can be considered as the recommended ones.

Table 3 presents the oscillator strengths for the transitions between the 3p^6 states of K I observed in the present work. When possible, we also included in Table 3 the f-values from the NIST database (Ralchenko et al. 2011). All of these NIST f-values were calculated using a Coulomb approximation (Anderson & Zilitis 1964); thus, as one would expect, the majority of these f-values are in good (within 10% accuracy) agreement with our QDT calculations, which also use the wave functions with Coulomb asymptotics.

Some transitions listed in this table were not observed in our experiment, and we present them for completeness only. We note that the intensities that are measured are not strictly proportional to the line strengths because the coefficient of this proportionality depends on the upper state population, even for the equilibrium population distribution. For example, in the 1100–1700 cm^{-1} range, the largest line strength corresponds to the 1343.699 cm^{-1} line, while, in our laser-ablated plasma, the 1548.559, 1556.986, and 1610.601 cm^{-1} lines appear to be much more prominent. However, in the solar ACE spectra (Hase et al. 2010), the 1548.559 and 1556.986 cm^{-1} lines are very weak compared to the 1343.699 cm^{-1} line (and the 1610.601 cm^{-1} line does not appear at all in the ACE spectra). Obviously the f-values are insufficient for an accurate determination of the intensities of solar lines, which are also determined by the populations of the atomic and ionic states in the line-forming regions of the solar photosphere.

4. Conclusion

While current and future satellite-based spectrometers are and will be capable of recording the IR spectra of various objects in almost the full IR range, there are great difficulties in analyzing laboratory IR spectroscopy for wavelengths longer than 5 microns. To our knowledge, there are no laboratory measured spectra of metals above 5.5 microns. In the present work, we have reported the results of an FTIR spectroscopy study of K I transitions in the IR wavelength ranges, 1.4–2.5, 2.7–5.0, 5.9–9.1, and 11.1–14.3 microns. We list 38 IR lines of K I (at a resolution of 0.017 cm^{-1}), 25 of which had not been previously experimentally observed in a laboratory. The recorded wave numbers are in good agreement with the data from the ACE solar spectrum. We corrected the ACE identification of three lines (1343.699, 1548.559, and 1556.986 cm^{-1}). From the 809.189, 1352.873, and 1343.698 cm^{-1} lines, we report the energy values of the 7h, 6g, and 6h levels, which had not been observed for K I. We also update the energies of another 23 K I levels, most of which had been reported some decades ago. The f-values calculated assuming the quantum-defect theory approximation are presented for the transitions involving the reported K I levels. Some of these f-values have not been previously calculated, while the others are in good agreement with the f-values available from the NIST database.

Table 4. Revised energy values (cm^{-1}) of some levels of K I.

Level	Present work	Other sources
7h	32768.775(27)	
6h	31961.001(10)	
6g	31959.583(20)	
$6f_{\frac{7}{2}}$	31953.141(11)	31953.17(6) (Risberg 1956)
$6f_{\frac{5}{2}}$	31953.154(9)	31953.17(6) (Risberg 1956)
$8s_{\frac{1}{2}}$	31765.377(3)	31765.3767(30) (Thompson et al. 1983)
$7p_{\frac{3}{2}}$	31074.378(14)	31074.40(6) (Risberg 1956)
$7p_{\frac{1}{2}}$	31069.865(19)	31069.90(6) (Risberg 1956)
5g	30617.306(8)	30617.31(1) (Litzen 1970)
$5f_{\frac{7}{2}}$	30606.710(8)	30606.73(6) (Risberg 1956)
$5f_{\frac{5}{2}}$	30606.700(9)	30606.73(6) (Risberg 1956)
$7s_{\frac{1}{2}}$	30274.252(3)	30274.2487(30) (Thompson et al. 1983)
$5d_{\frac{3}{2}}$	30185.748(3)	30185.7476(30) (Thompson et al. 1983)
$5d_{\frac{5}{2}}$	30185.244(3)	30185.244(3) (Thompson et al. 1983)
$6p_{\frac{3}{2}}$	29007.685(3)	29007.71(5) (Risberg 1956)
$6p_{\frac{1}{2}}$	28999.262(4)	28999.27(5) (Risberg 1956)
$4f_{\frac{7}{2}}$	28127.855(4)	28127.85(5) (Risberg 1956)
$4f_{\frac{5}{2}}$	28127.865(4)	28127.85(5) (Risberg 1956)
$6s_{\frac{1}{2}}$	27450.701(2)	27450.7104(30) (Thompson et al. 1983)
$4d_{\frac{3}{2}}$	27398.152(4)	27398.147(5) (Johansson & Svendenius 1972)
$4d_{\frac{5}{2}}$	27397.079(3)	27397.077(5) (Johansson & Svendenius 1972)
$5p_{\frac{3}{2}}$	24720.142(3)	24720.139(5) (Johansson & Svendenius 1972)
$5p_{\frac{1}{2}}$	24701.390(3)	24701.382(5) (Johansson & Svendenius 1972)
$3d_{\frac{3}{2}}$	21536.997(4)	21536.988(5) (Johansson & Svendenius 1972)
$3d_{\frac{5}{2}}$	21534.683(4)	21534.680(5) (Johansson & Svendenius 1972)
$5s_{\frac{1}{2}}$	21026.560(4)	21026.551(5) (Johansson & Svendenius 1972)

Acknowledgements. This work was financially supported by the Grant Agency of the Academy of Sciences of the Czech Republic (grant No. IAA400400705), by the Ministry of Finance of the Czech Republic (Project ECPF:049/4V) and the Ministry of Education, Youth, and Sports of the Czech Republic (grant No. LM2010014).

References

Akindinova, E. V., Chernov, V. E., Kretinin, I. Y., & Zon, B. A. 2009, Phys. Rev. A, 79, 032506
Alcheev, P. G., Chernov, V. E., & Zon, B. A. 2002, J. Mol. Spectrosc., 211, 71
Anderson, E. M., & Zilitis, V. A. 1964, Opt. Spectrosk., 16, 177
Asplund, M., Grevesse, N., Sauval, A. J., & Scott, P. 2009, ARA&A, 47, 481

Biémont, E. 1994, in Infrared Solar Physics, ed. D. M. Rabin, J. T. Jefferies, & C. Lindsey, Int. Astron. Union (Dordrecht, The Netherlands: Kluwer Academic Publ.), 501, 154th Symposium of the International-Astronomical-Union, 1st International Meeting devoted to Infrared Physics, Tucson, AZ, Mar. 02–06, 1992, IAU Symp., 154,
Blackwell-Whitehead, R. J., Pickering, J. C., Pearse, O., & Nave, G. 2005, ApJS, 157, 402
Blackwell-Whitehead, R., Pavlenko, Y. V., Nave, G., et al. 2011, A&A, 525, A44
Brown, M. S., Federman, S. R., Irving, R. E., Cheng, S., & Curtis, L. J. 2009, ApJ, 702, 880
Chernov, V. E., Dorofeev, D. L., Kretinin, I. Y., & Zon, B. A. 2005, Phys. Rev. A, 71, 022505
Civiš, S., Matulková, I., Cihelka, J., et al. 2010a, Phys. Rev. A, 81, 012510
Civiš, S., Matulková, I., Cihelka, J., et al. 2010b, Phys. Rev. A, 82, 022502
Civiš, S., Kubelík, P., Jelínek, P., Chernov, V. E., & Knyazev, M. Y. 2011a, J. Phys. B, 44, 225006
Civiš, S., Matulková, I., Cihelka, J., et al. 2011b, J. Phys. B, 44, 105002
Civiš, S., Matulková, I., Cihelka, J., et al. 2011c, J. Phys. B, 44, 025002
Deb, N. C., & Hibbert, A. 2010, ApJ, 711, L104
Farmer, C. B., Norton, R. H., & Geller, M. 1989, NASA Reference Publication, 1224
Gehren, T., Butler, K., Mashonkina, L., Reetz, J., & Shi, J. 2001, A&A, 366, 981
Gehrz, R., Becklin, E., de Pater, I., et al. 2009, Adv. Space Res., 44, 413
Giacomo, A. D., Shakhatov, V., & Pascale, O. D. 2001, Spectrochimica Acta Part B: Atomic Spectroscopy, 56, 753, 1st International Conference on Laser-Induced Plasma Spectroscopy and Applications (LIBS 2000), Tirrenia, Italy, Oct. 08–12, 2000
Goicoechea, J. R., Nakagawa, T., & on behalf of the SAFARI/SPICA teams 2011, in Conditions and impact of star formation: New results with Herschel and beyond, The 5th Zermatt ISM Symposium (EDP Sciences)
Goldman, A., Blatherwick, R. D., Murcray, F. J., & Murcray, D. G. 1996, Appl. Opt., 35, 2821
Grevesse, N., & Noels, A. 1994, Phys. Scr., T51, 47
Hase, F., Wallace, L., McLeod, S. D., Harrison, J. J., & Bernath, P. F. 2010, J. Quant. Spec. Radiat. Transf., 111, 521
Houck, J. R., Roellig, T. L., van Cleve, J., et al. 2004, ApJS, 154, 18
Johansson, S. 2005, in High Resolution Infrared Spectroscopy In Astronomy, Proceedings, ed. H. U. Kaufl, R. Siebenmorgen, & A. Moorwood, ESO Astrophysics Symposia, ESO (Heidelberger Berlin, Germany: Springer–Verlag Berlin), 62, ESO Workshop on High Resolution Infrared Spectroscopy in Astronomy, Garching, Germany, Nov. 18–21, 2003
Johansson, I., & Svendenius, N. 1972, Phys. Scr., 5, 129
Jorissen, A. 2004, Phys. Scr., T112, 73
Kawaguchi, K., Hama, Y., & Nishida, S. 2005, J. Mol. Spectrosc., 232, 1
Kawaguchi, K., Sanechika, N., Nishimura, Y., et al. 2008, Chem. Phys. Lett., 463, 38
Kerber, F., Nave, G., Sansonetti, C. J., & Bristow, P. 2009, Phys. Scr., T134, 014007
Kurucz, R. L. 2011, Can. J. Phys., 89, 417
Larsson, M. 1983, A&A, 128, 291
Litzen, U. 1970, Phys. Scr., 1, 253
Lobel, A. 2011, Can. J. Phys., 89, 395
Lodders, K. 2003, ApJ, 591, 1220
Lyubchik, Y., Jones, H., Pavlenko, Y., et al. 2004, A&A, 416, 655
Lyubchik, Y., Jones, H. R. A., Pavlenko, Y. V., et al. 2007, A&A, 473, 257
Manrique, J., Aguilera, J., & Aragón, C. 2011, J. Quant. Spec. Radiat. Transf., 112, 85
McGovern, M. R., Kirkpatrick, J. D., McLean, I. S., et al. 2004, ApJ, 600, 1020
McLean, I., McGovern, M., Burgasser, A., et al. 2003, ApJ, 596, 561
Murakami, H., Baba, H., Barthel, P., et al. 2007, PASJ, 59, S369
Nilsson, H. 2009, Phys. Scr., T134, 014009
OPUS 2010, Opus Spectroscopy Software, http://www.brukeroptics.com/opus.html
Pickering, J. C. 1999, Phys. Scr., T83, 27
Pickering, J., Blackwell-Whitehead, R., Thorne, A., Ruffoni, M., & Holmes, C. 2011, Can. J. Phys., 89, 387
Raassen, A. J. J., Pickering, J. C., & Uylings, P. H. M. 1998, A&AS, 130, 541
Ralchenko, Y., Kramida, A., Reader, J., & NIST ASD Team 2011, NIST Atomic Spectra Database (version 4.1.0)
Richter, M. J., Ennico, K. A., McKelvey, M. E., & Seifahrt, A. 2010, Proc. SPIE, 7735, 77356Q
Risberg, P. 1956, Ark. Fys. (Stockholm), 10, 583
Ryde, N. 2010, Astron. Nachr., 331, 433
Shabanova, L. N., & Khlyustalov, A. N. 1985a, Opt. Spectrosk., 59, 207,
Shabanova, L. N., & Khlyustalov, A. N. 1985b, Opt. Spectrosc., 59, 123
Stuart, B. H. 2004, Infrared Spectroscopy: Fundamentals and Applications (Analytical Techniques in the Sciences (AnTs), 1st edn. (Wiley)
Sylwester, J., Sylwester, B., Phillips, K. J. H., & Kuznetsov, V. D. 2010, ApJ, 710, 804
Thompson, D. C., O'Sullivan, M. S., Stoicheff, B. P., & Xu, G. X. 1983, Can. J. Phys., 61, 949
Thorne, A. P., Pickering, J. C., & Semeniuk, J. 2011, ApJS, 192, 11
Villars, D. S. 1952, J. Opt. Soc. Am., 42, 552
Wahlgren, G. M. 2011, Can. J. Phys., 89, 345
Wallace, L., & Hinkle, K. 2007, ApJS, 169, 159
Wallace, L., & Hinkle, K. 2009, ApJ, 700, 720
Wallace, L., Livingston, W., Hinkle, K., & Bernath, P. 1996, ApJS, 106, 165
Wang, H., Li, J., Wang, X. T., et al. 1997, Phys. Rev. A, 55, R1569
Zhang, H. W., Butler, K., Gehren, T., Shi, J. R., & Zhao, G. 2006a, A&A, 453, 723
Zhang, H. W., Gehren, T., Butler, K., Shi, J. R., & Zhao, G. 2006b, A&A, 457, 645

Table 3. Calculated oscillator strengths, f_{ik}, for the transitions between the $3p^6$ states of K I observed in the present work.

Transition	ν (cm^{-1})	λ (μ)m	log($g_i f_{ik}$) (QDT)	f_{ik} QDT	f_{ik} NIST
$3d_{\frac{5}{2}}$–$6f_{\frac{5}{2}}$	10 418.47	959.571	−3.86	3.52×10^{-3}	3.3×10^{-3}
$3d_{\frac{5}{2}}$–$6f_{\frac{7}{2}}$	10 418.456	959.572	−0.863	7.03×10^{-2}	6.4×10^{-2}
$3d_{\frac{3}{2}}$–$6f_{\frac{5}{2}}$	10 416.157	959.784	−1.22	7.38×10^{-2}	6.8×10^{-2}
$5s_{\frac{1}{2}}$–$7p_{\frac{3}{2}}$	10 047.818	994.968	−4.94	3.57×10^{-3}	4.2×10^{-3}
$5s_{\frac{1}{2}}$–$7p_{\frac{1}{2}}$	10 043.305	995.415	−5.71	1.66×10^{-3}	2.1×10^{-3}
$3d_{\frac{5}{2}}$–$7p_{\frac{3}{2}}$	9539.695	1047.96	−4.26	2.35×10^{-3}	1.9×10^{-3}
$3d_{\frac{3}{2}}$–$7p_{\frac{3}{2}}$	9537.381	1048.22	−6.46	3.92×10^{-4}	3.1×10^{-4}
$3d_{\frac{3}{2}}$–$7p_{\frac{1}{2}}$	9532.868	1048.71	−4.86	1.93×10^{-3}	1.6×10^{-3}
$3d_{\frac{5}{2}}$–$5f_{\frac{7}{2}}$	9072.024	1101.99	+0.0545	1.76×10^{-1}	1.6×10^{-1}
$3d_{\frac{5}{2}}$–$5f_{\frac{5}{2}}$	9072.013	1101.99	−2.94	8.78×10^{-3}	8.0×10^{-3}
$3d_{\frac{3}{2}}$–$5f_{\frac{5}{2}}$	9069.7	1102.27	−0.307	1.84×10^{-1}	1.7×10^{-1}
$5s_{\frac{1}{2}}$–$6p_{\frac{3}{2}}$	7981.119	1252.61	−3.23	1.98×10^{-2}	2.1×10^{-2}
$5s_{\frac{1}{2}}$–$6p_{\frac{1}{2}}$	7972.695	1253.94	−3.97	9.42×10^{-3}	1.1×10^{-2}
$3d_{\frac{5}{2}}$–$6p_{\frac{3}{2}}$	7473.001	1337.78	−3.05	7.88×10^{-3}	6.6×10^{-3}
$3d_{\frac{3}{2}}$–$6p_{\frac{3}{2}}$	7470.688	1338.2	−5.25	1.31×10^{-3}	1.1×10^{-3}
$3d_{\frac{3}{2}}$–$6p_{\frac{1}{2}}$	7462.264	1339.71	−3.65	6.48×10^{-3}	5.5×10^{-3}
$5p_{\frac{1}{2}}$–$8s_{\frac{1}{2}}$	7063.987	1415.24	−4.04	8.84×10^{-3}	8.7×10^{-3}
$5p_{\frac{3}{2}}$–$8s_{\frac{1}{2}}$	7045.235	1419.01	−3.35	8.77×10^{-3}	8.8×10^{-3}
$3d_{\frac{5}{2}}$–$4f_{\frac{5}{2}}$	6593.18	1516.3	−1.45	3.92×10^{-2}	3.4×10^{-2}
$3d_{\frac{5}{2}}$–$4f_{\frac{7}{2}}$	6593.17	1516.31	+1.55	7.85×10^{-1}	6.9×10^{-1}
$3d_{\frac{3}{2}}$–$4f_{\frac{5}{2}}$	6590.867	1516.84	+1.19	8.24×10^{-1}	7.8×10^{-1}
$5p_{\frac{1}{2}}$–$7s_{\frac{1}{2}}$	5572.862	1793.92	−2.92	2.71×10^{-2}	2.7×10^{-2}
$5p_{\frac{3}{2}}$–$7s_{\frac{1}{2}}$	5554.11	1799.98	−2.23	2.70×10^{-2}	2.7×10^{-2}
$5p_{\frac{1}{2}}$–$5d_{\frac{3}{2}}$	5484.357	1822.87	−4.2	7.49×10^{-3}	7.8×10^{-3}
$5p_{\frac{3}{2}}$–$5d_{\frac{3}{2}}$	5465.605	1829.12	−5.9	6.83×10^{-4}	8.0×10^{-4}
$5p_{\frac{3}{2}}$–$5d_{\frac{5}{2}}$	5465.101	1829.29	−3.71	6.10×10^{-3}	7.1×10^{-3}
$4d_{\frac{5}{2}}$–$6f_{\frac{5}{2}}$	4556.075	2194.27	−3.22	6.65×10^{-3}	6.7×10^{-3}
$4d_{\frac{5}{2}}$–$6f_{\frac{7}{2}}$	4556.061	2194.28	−0.226	1.33×10^{-1}	1.3×10^{-1}
$4d_{\frac{3}{2}}$–$6f_{\frac{5}{2}}$	4555.001	2194.79	−0.58	1.40×10^{-1}	1.4×10^{-1}
$4f_{\frac{7}{2}}$–$6g_{\frac{9}{2}}$	3831.728	2609.08	+0.365	1.80×10^{-1}	
$4f_{\frac{7}{2}}$–$6g_{\frac{7}{2}}$	3831.728	2609.08	−3.19	5.15×10^{-3}	
$4f_{\frac{5}{2}}$–$6g_{\frac{7}{2}}$	3831.718	2609.08	+0.104	1.85×10^{-1}	
$5s_{\frac{1}{2}}$–$5p_{\frac{3}{2}}$	3693.577	2706.66	+0.669	9.76×10^{-1}	1.0
$4d_{\frac{5}{2}}$–$7p_{\frac{3}{2}}$	3677.299	2718.65	−2.09	2.06×10^{-2}	1.8×10^{-2}
$4d_{\frac{3}{2}}$–$7p_{\frac{3}{2}}$	3676.226	2719.44	−4.29	3.44×10^{-3}	3.1×10^{-3}
$5s_{\frac{1}{2}}$–$5p_{\frac{1}{2}}$	3674.825	2720.48	−0.0263	4.87×10^{-1}	5.0×10^{-1}
$4d_{\frac{3}{2}}$–$7p_{\frac{1}{2}}$	3671.713	2722.78	−2.69	1.70×10^{-2}	1.6×10^{-2}
$6s_{\frac{1}{2}}$–$7p_{\frac{3}{2}}$	3623.677	2758.88	−2.72	3.31×10^{-2}	
$6s_{\frac{1}{2}}$–$7p_{\frac{1}{2}}$	3619.164	2762.32	−3.45	1.59×10^{-2}	
$4d_{\frac{5}{2}}$–$5f_{\frac{7}{2}}$	3209.629	3114.78	+0.858	3.93×10^{-1}	3.9×10^{-1}
$4d_{\frac{5}{2}}$–$5f_{\frac{5}{2}}$	3209.618	3114.79	−2.14	1.97×10^{-2}	1.9×10^{-2}
$4d_{\frac{3}{2}}$–$5f_{\frac{5}{2}}$	3208.544	3115.83	+0.502	4.13×10^{-1}	4.2×10^{-1}
$3d_{\frac{5}{2}}$–$5p_{\frac{3}{2}}$	3185.459	3138.41	−0.0661	1.56×10^{-1}	1.4×10^{-1}
$3d_{\frac{3}{2}}$–$5p_{\frac{3}{2}}$	3183.146	3140.69	−2.26	2.61×10^{-2}	2.2×10^{-2}
$3d_{\frac{3}{2}}$–$5p_{\frac{1}{2}}$	3164.394	3159.3	−0.646	1.31×10^{-1}	1.1×10^{-1}
$6p_{\frac{1}{2}}$–$8s_{\frac{1}{2}}$	2766.115	3614.19	−2.62	3.65×10^{-2}	
$6p_{\frac{3}{2}}$–$8s_{\frac{1}{2}}$	2757.692	3625.23	−1.93	3.62×10^{-2}	
$5p_{\frac{1}{2}}$–$6s_{\frac{1}{2}}$	2749.309	3636.29	−0.462	3.15×10^{-1}	3.2×10^{-1}
$5p_{\frac{3}{2}}$–$6s_{\frac{1}{2}}$	2730.557	3661.26	+0.237	3.17×10^{-1}	3.2×10^{-1}
$5p_{\frac{1}{2}}$–$4d_{\frac{3}{2}}$	2696.762	3707.14	+0.892	1.22	1.2
$5p_{\frac{3}{2}}$–$4d_{\frac{3}{2}}$	2678.01	3733.1	−0.717	1.22×10^{-1}	1.2×10^{-1}
$5p_{\frac{3}{2}}$–$4d_{\frac{5}{2}}$	2676.936	3734.6	+1.47	1.09	1.1
$4f_{\frac{7}{2}}$–$5g_{\frac{7}{2}}$	2489.451	4015.85	−1.21	3.73×10^{-2}	
$4f_{\frac{7}{2}}$–$5g_{\frac{9}{2}}$	2489.451	4015.85	+2.34	1.30	

Table 3. continued.

Transition	ν (cm^{-1})	λ (μm)	$\log(g_i f_{ik})$ (QDT)	f_{ik} QDT	f_{ik} NIST
$4f_{\frac{5}{2}}$–$5g_{\frac{7}{2}}$	2489.441	4015.87	+2.08	1.34	
$5g_{\frac{9}{2}}$–$7h_{\frac{9}{2}}$	2151.469	4646.72	−3.3	3.69×10^{-3}	
$5g_{\frac{9}{2}}$–$7h_{\frac{11}{2}}$	2151.469	4646.72	+0.688	1.99×10^{-1}	
$5g_{\frac{7}{2}}$–$7h_{\frac{9}{2}}$	2151.469	4646.72	+0.485	2.03×10^{-1}	
$4f_{\frac{5}{2}}$–$5d_{\frac{3}{2}}$	2057.884	4858.04	−1.07	5.69×10^{-2}	
$4f_{\frac{7}{2}}$–$5d_{\frac{5}{2}}$	2057.39	4859.2	−0.717	6.10×10^{-2}	
$4f_{\frac{5}{2}}$–$5d_{\frac{5}{2}}$	2057.38	4859.23	−3.71	4.07×10^{-3}	
$5d_{\frac{5}{2}}$–$6f_{\frac{5}{2}}$	1767.91	5654.85	−2.66	1.16×10^{-2}	
$5d_{\frac{5}{2}}$–$6f_{\frac{7}{2}}$	1767.896	5654.9	+0.331	2.32×10^{-1}	
$5d_{\frac{3}{2}}$–$6f_{\frac{5}{2}}$	1767.406	5656.47	−0.0243	2.44×10^{-1}	
$4d_{\frac{5}{2}}$–$6p_{\frac{3}{2}}$	1610.606	6207.15	+0.627	3.12×10^{-1}	3.0×10^{-1}
$4d_{\frac{3}{2}}$–$6p_{\frac{3}{2}}$	1609.532	6211.29	−1.57	5.21×10^{-2}	5.0×10^{-2}
$4d_{\frac{3}{2}}$–$6p_{\frac{1}{2}}$	1601.108	6243.97	+0.0431	2.61×10^{-1}	2.4×10^{-1}
$6s_{\frac{1}{2}}$–$6p_{\frac{3}{2}}$	1556.985	6420.92	+0.94	1.28	
$6s_{\frac{1}{2}}$–$6p_{\frac{1}{2}}$	1548.561	6455.85	+0.248	6.41×10^{-1}	
$5f_{\frac{5}{2}}$–$6g_{\frac{7}{2}}$	1352.883	7389.61	+1.95	1.17	
$5f_{\frac{7}{2}}$–$6g_{\frac{9}{2}}$	1352.873	7389.66	+2.21	1.14	
$5f_{\frac{7}{2}}$–$6g_{\frac{7}{2}}$	1352.873	7389.66	−1.35	3.25×10^{-2}	
$5g_{\frac{7}{2}}$–$6h_{\frac{9}{2}}$	1343.698	7440.12	+2.6	1.68	
$5g_{\frac{9}{2}}$–$6h_{\frac{11}{2}}$	1343.698	7440.12	+2.8	1.65	
$5g_{\frac{9}{2}}$–$6h_{\frac{9}{2}}$	1343.698	7440.12	−1.19	3.05×10^{-2}	
$5g_{\frac{7}{2}}$–$6f_{\frac{5}{2}}$	1335.849	7483.84	−2.77	7.85×10^{-3}	
$5g_{\frac{7}{2}}$–$6f_{\frac{7}{2}}$	1335.835	7483.91	−6.06	2.91×10^{-4}	
$5g_{\frac{9}{2}}$–$6f_{\frac{7}{2}}$	1335.835	7483.91	−2.51	8.14×10^{-3}	
$6p_{\frac{1}{2}}$–$7s_{\frac{1}{2}}$	1274.99	7841.06	−0.0965	4.54×10^{-1}	
$6p_{\frac{3}{2}}$–$7s_{\frac{1}{2}}$	1266.567	7893.21	+0.601	4.56×10^{-1}	
$6p_{\frac{1}{2}}$–$5d_{\frac{3}{2}}$	1186.487	8425.95	+1.12	1.53	
$6p_{\frac{3}{2}}$–$5d_{\frac{3}{2}}$	1178.063	8486.2	−0.491	1.53×10^{-1}	
$6p_{\frac{3}{2}}$–$5d_{\frac{5}{2}}$	1177.559	8489.83	+1.71	1.38	
$5d_{\frac{5}{2}}$–$7p_{\frac{3}{2}}$	889.134	11 243.8	+1.02	4.64×10^{-1}	
$5d_{\frac{3}{2}}$–$7p_{\frac{3}{2}}$	888.63	11 250.2	−1.17	7.74×10^{-2}	
$5d_{\frac{3}{2}}$–$7p_{\frac{1}{2}}$	884.117	11 307.6	+0.44	3.88×10^{-1}	
$6g_{\frac{9}{2}}$–$7h_{\frac{9}{2}}$	809.192	12 354.6	−1.3	2.72×10^{-2}	
$6g_{\frac{9}{2}}$–$7h_{\frac{11}{2}}$	809.192	12 354.6	+2.69	1.47	
$6g_{\frac{7}{2}}$–$7h_{\frac{9}{2}}$	809.192	12 354.6	+2.48	1.50	
$7s_{\frac{1}{2}}$–$7p_{\frac{3}{2}}$	800.126	12 494.6	+1.14	1.57	
$7s_{\frac{1}{2}}$–$7p_{\frac{1}{2}}$	795.613	12 565.5	+0.454	7.87×10^{-1}	
$4d_{\frac{5}{2}}$–$4f_{\frac{5}{2}}$	730.785	13 680.2	−2.25	1.76×10^{-2}	1.7×10^{-2}
$4d_{\frac{5}{2}}$–$4f_{\frac{7}{2}}$	730.775	13 680.4	+0.75	3.53×10^{-1}	3.3×10^{-1}
$4d_{\frac{3}{2}}$–$4f_{\frac{5}{2}}$	729.711	13 700.3	+0.392	3.70×10^{-1}	3.5×10^{-1}
$7p_{\frac{1}{2}}$–$8s_{\frac{1}{2}}$	695.512	14 374.0	+0.167	5.91×10^{-1}	
$7p_{\frac{3}{2}}$–$8s_{\frac{1}{2}}$	690.999	14 467.9	+0.864	5.93×10^{-1}	
$5d_{\frac{5}{2}}$–$5f_{\frac{7}{2}}$	421.464	23 720.4	+1.42	6.87×10^{-1}	
$5d_{\frac{5}{2}}$–$5f_{\frac{5}{2}}$	421.453	23 721.	−1.58	3.43×10^{-2}	
$5d_{\frac{3}{2}}$–$5f_{\frac{5}{2}}$	420.949	23 749.4	+1.06	7.20×10^{-1}	

Notes. The Ritz wavenumbers, ν, and air wavelengths, λ, are calculated using the energy values taken from the present measurement (see Table 4). The NIST f-values (last column) were calculated using a Coulomb approximation (Anderson & Zilitis 1964).